Identification of montmorillonite particle edge orientations by atomic-force microscopy

Sergey Kraevsky, Christophe Tournassat, Marylène Vayer, Fabienne Warmont, Sylvain Grangeon, Brice F. Ngouana Wakou, Andrey G. Kalinichev

Identification of montmorillonite particle edge orientations by atomic-force microscopy

Sergey V. Kraevsky [1,2,3,4,*], Christophe Tournassat[2,5,6], Marylène Vayer[7], Fabienne Warmont[7], Sylvain Grangeon[2], Brice F. Ngouana Wakou[1], and Andrey G. Kalinichev[1,8]

[1] Laboratoire SUBATECH (UMR 6457 - Institut Mines-Télécom Atlantique, Université de Nantes, CNRS/IN2P3), 44307 Nantes, France

[2] BRGM, 3 avenue Claude Guillemin, 45060 Orléans, France

[3] Kurchatov Institute - ITEP, 117218 Moscow, Russian Federation

[4] Federal Research and Clinical Center of Physical-Chemical Medicine, 119435, Moscow, Russian Federation

[5] Université d'Orléans – CNRS/INSU – BRGM, UMR 7327 Institut des Sciences de la Terre d'Orléans, 45071 Orléans, France

[6] Lawrence Berkeley National Laboratory, 1 Cyclotron Road, Berkeley, CA 94720, USA

[7] ICMN-CNRS-Université d'Orléans, 1b rue de la Férollerie, 45071 Orléans Cedex 2, France

[8] National Research University Higher School of Economics, Moscow, Russian Federation

*Corresponding author: Sergey V. Kraevsky (s.kraevsky@rcpcm.org)

ABSTRACT

Statistical information on the edge surface area and edge crystallographic orientation of clay nanoparticle surfaces is essential for proper accounting of the protonation-deprotonation reactions as a part of mechanistic surface complexation models. A combination of atomic-force microscopy (AFM) measurements and molecular dynamics computer simulations made it possible to quantify the relative contributions of the most frequently occurring montmorillonite edge surfaces to the total edge surface area. Edge surfaces normal to the [110] and [010] crystallographic directions are found to be the most abundant (~60% and ~20%, respectively), in agreement with previous estimations.

Keywords: clay nanoparticles, montmorillonite, edges ratio, AFM, MD simulations

INTRODUCTION

The adsorption and resulting retardation of many contaminants by clay minerals make them ideal for use in natural or engineered barrier systems (ANDRA, 2005; Gates et al. 2009; Marty et al., 2010). The determination of a macroscopic retardation coefficient is a first step towards the quantification of sorption and thus retardation of ions by mineral surfaces, but a sound mechanistic understanding of the molecular-scale interaction between ions and surfaces is mandatory to the building of reliable geochemical models (Tournassat et al., 2013; Borisover and Davis, 2015). However, accurate mechanistic modeling of ion adsorption on clay mineral surfaces remains challenging because of the diversity of adsorption sites on the basal and edge surfaces of clay mineral particles (Churakov, 2006). The view that the acid-base properties of amphoteric groups at the edge surfaces as well as the free energy of specific adsorption of cations (Ni^{2+}, UO_2^{2+}, *etc*.) are dependent on the crystallographic orientation of the surface (Everett, 1998) is supported by *ab initio* molecular dynamics (MD) computer simulations (Churakov, 2006; Liu et al., 2008, 2012, 2013, 2014, 2015a,b; Zhang et al., 2017), and the construction of mechanistic surface complexation models (SCM) for clay minerals thus necessitates to have a statistical information on the edge surface area and edge crystallographic orientation of clay mineral layer surfaces (Bourg et al., 2007, Tournassat et al., 2016, Zhang et al., 2018). In the present study, we focused our efforts on montmorillonite, *i.e.* the dioctahedral smectite of which the adsorption properties have been the most studied in the literature.

Previous classical and *ab initio* molecular dynamics (MD) simulations of hydrated montmorillonite edges suggested that the nanoparticle surfaces normal to the [110] crystallographic direction may be significantly more stable than the surfaces normal to the [010] direction (Bickmore et al, 2003; Churakov, 2006; Newton et al, 2015, 2016; Kwon and Newton, 2016). Cleavage energies (ΔE) and corresponding Gibbs free energies (ΔG) for edge surfaces predicted by density functional theory (DFT) are also in agreement with these findings. For example, Lavikainen at al. (2015) calculated that the ratio of (110), (010) and (100) edge surfaces of pyrophillite, an uncharged

clay mineral with a layer structure similar to montmorillonite, is 69%, 29%, and 2%, respectively, while the (130) edge surface represents less than 1% of the total surface area. However, montmorillonite layers exhibit significant differences with the pyrophyllite layers. First of all, montmorillonite layers are negatively charged due to the presence of isomorphic substitutions in their octahedral and tetrahedral sheets. Secondly, pyrophyllite has a trans-vacant layer structure, while most montmorillonite samples have a cis-vacant layer structure (Tsipursky and Drits, 1984). Hence, the relative proportions of different edge faces contributing to the total surface area of the charged montmorillonite nanoparticles is still largely unknown.

Numerous recent atomic force microscopy (AFM) studies of different clays prove the possibility to achieve a real atomic scale resolution of clay structures. For instance, Ferrage et al. (2006) used X-ray and electron diffraction for the interpretation of their AFM atomic scale images. Siretanu et al. (2016), studied surface defects of different clay materials, including montmorillonite, and demonstrated that AFM can provide insights on the morphology and atomic scale structure of clay layers.

At the same time, atomistic computer simulations have been already demonstrated to be very insightful in interpreting the AFM images of hydrated mineral surfaces enabling one to clarify the underlying imaging mechanism in the AFM experiments (Kobayashi et al., 2016; Umeda et al., 2017; Reischl et al., 2019).

In the present work, we used AFM experiments for visualization and quantitative characterization of the geometry and size distribution of montmorillonite particles, as well as for reliable determination of the crystallographic orientation of their edges. Fourier peaks of the AFM-images were then decoded using the insight from the atomistic computer simulations of the same systems.

MATERIALS AND METHODS

Clay mineral

The Kunipia-P sample used in this study is a purified Na-montmorillonite produced by Kunimine industries Co. Ltd., and which contains nearly 100% montmorillonite (Tachi and Yotsuji, 2014; Orucoglu et al. 2018). Kunipia-P montmorillonite was dispersed in deionized water at a solid concentration of 0.01 g L^{-1} and ultrasonicated for 10 min. A droplet of the dispersion was then deposited on a freshly cleaved mica surface (purity grade V1, Ted Pella, Inc.) and dried overnight in a desiccator.

AFM samples preparation

AFM measurements were carried out with samples mounted in dry- and fluid-cells using a Dimension Icon AFM (Bruker) microscope in contact and peak force modes. The AFM images were obtained in air with lateral force microscopy - friction data channel (Erlandsson et al., 1988; Marti et al., 1990), using SNL-10 silicon nitride cantilevers (Bruker Inc.). The scan parameters were: rate 5 Hz, angle 0, gains 0.3. Particles perimeter and surface area were estimated by processing the AFM image using the FemtoScan (Filonov et al., 2001) and ImageJ (https://imagej.nih.gov) softwares.

Montmorillonite and muscovite structural models for MD simulations

Classical MD simulations were performed with the LAMMPS software (Plimpton, 1995) for a montmorillonite model that was built from an orthogonal pyrophyllite structure (Drits *et al.*, 2012), by randomly distributing Al/Si and Mg/Al isomorphic substitutions (Ngouana and Kalinichev, 2014) in the tetrahedral and octahedral sheets of the layers, respectively. The simulation supercell had dimensions of 4.1×3.6×10.5 nm^3 and contained a montmorillonite clay particle consisting of three T-O-T layers, each having 32 unit cells with the chemical composition $[Si_{7.75}Al_{0.25}][Al_{3.5}Mg_{0.5}]O_{20}(OH)_4Na_{0.75}(H_2O)_{10}]$, in which the layer charge of -0.75|*e*| per unit cell was neutralized by Na^+ ions. The layer-to-layer distance was selected and fixed to represent a bilayer hydrate of Na-montmorillonite, with 10 H_2O/Na^+ in each of the interlayers (Ngouana and

Kalinichev, 2014). The remaining volume of the simulation box was filled with 3280 H_2O molecules to represent the interfacial liquid water at a density of 1 g/cm^3, corresponding to ambient conditions (Fig.1).

The muscovite model for classical MD simulations was built similarly from the same orthogonal pyrophyllite structure (Drits *et al.*, 2012) by randomly distributing Al/Si isomorphic substitutions in the tetrahedral sheets of the clay layers to achieve the chemical composition of $[Si_6Al_2][Al_4]O_{20}(OH)_4K_2$] (see, e.g., Loganathan and Kalinichev, 2017). The simulation supercell was a little shorter and had the dimensions of 4.1×3.6×8.5 nm^3. The layer charge of -2.0|*e*| per unit cell was neutralized by the corresponding number of interlayer and interfacial K^+ ions and the rest of the simulation cell was filled with 2960 H_2O molecules to achieve the liquid water density of 1 g/cm^3, corresponding to ambient conditions (Fig.1).

MD simulations parameters and procedure

For both montmorillonite and muscovite models, the MD simulation protocol was the same. The ClayFF force field (Cygan *et al.*, 2004) was used to calculate all the interatomic interactions for each model. Periodic boundary conditions were applied and Ewald summation was used to account for the long range electrostatic interactions in the system. The equations of atomic motion were numerically integrated using a time step of 1 fs and each model was initially equilibrated under ambient conditions (T = 300 K, P = 1 bar) during a 1 ns MD run in the *NPT* statistical ensemble, followed by an additional 0.5 ns equilibration run in the *NVT* ensemble, before a 1 ns *NVT* production MD run was started. The results of that equilibrium *NVT* MD run were then statistically analyzed to extract various properties of the simulated systems.

RESULTS AND DISCUSSION

Montmorillonite particle size and shape measurements

A few individual particles of montmorillonite had a lath-like shape, which is typical for mica crystals (Bauer et al., 2000; Güven, 2001) (Fig. 2). Some other montmorillonite particles had fairly well defined straight boundaries, which suggests that they belonged to certain crystallographic directions (Fig. 2 and 3).

To facilitate the calculation of the total edge surface area from the AFM images, the concentration of montmorillonite was selected during sample preparation so that its particles occupied the maximum area on the surface of the substrate but did not overlap each other (Fig. 3a). Because most of the particles imaged by AFM were montmorillonite single layer particles (Fig. 3), the edge specific surface area (SSA_{Edge}) was estimated from the computation of the perimeter to area ratio (Tournassat et al., 2003, Yokohama et al., 2005, Le Forestier et al., 2010, Marty et al., 2011, Reinholdt et al., 2013):

$$SSA_{Edge} = \frac{Ph}{m} = \frac{Ph}{S_b h \rho} = \frac{P}{S_b} \times \frac{1}{\rho} \quad (2)$$

where P is the perimeter (m), h the height (m), S_b the basal surface area (m^2) and ρ the density (kg/m^3) of the particle.

Montmorillonite particles do have a size distribution associated with the nature of montmorillonite and the distribution of surface charge (Assemi et al., 2015). The range of values of the P/S_b parameter calculated from more than 500 observed montmorillonite particles is shown on Figure 3b. The strongest variations were observed for smaller particles with a basal area of less than 0.1 μm^2 (about 20% of total) and the sub-range from particle to particle varied between 13-59 μm^{-1}. Approximately 60% of the particles had basal surface area in the range of 0.1-0.4 μm^2, their P/S_b parameter varied in the range of 8-13 μm^{-1}. The remaining 20% of the particles had a basal area of more than 0.4 μm^2, their P/S_b varies from 4-8 μm^{-1}.

A small but significant difference between the *dry*- and *fluid-cell* samples, 4.7±0.3 $m^2\ g^{-1}$ and 4.1±0.2 $m^2\ g^{-1}$, respectively, was observed. Very small particles may have been less strongly attached to the mica substrate surface in the presence of liquid than larger particles. Consequently, small particles with the highest perimeter to area ratio may have been lost. Assuming that the density of montmorillonite is about 2.7-2.8 g cm^{-3} (Tournassat and Appelo, 2011), SSA_{Edge} of Kunipia-P particles was estimated to be ~ 4.3±0.2 $m^2\ g^{-1}$, in good agreement with a previously reported value for a similar material, 5.3 $m^2\ g^{-1}$ (Yokoyama et al., 2005).

Crystallographic orientation of montmorillonite particle edge surfaces

AFM images taken at high resolution evidenced structures with a period of ~ 0.45 nm when scanning from top to bottom and ~ 0.51 nm when scanning from bottom to top. The interpretation of such atomic-resolution AFM images should be done however with extreme care due to the possibility of instrumental artefacts such as vibration noise or piezo ceramic hysteresis (e.g., Rodriguez-Fortun et al., 2011). To confirm that the periodic signal being analyzed actually corresponds to the crystallographic structure of the particle and does not represent a periodic noise, a series of control experiments with rotation of scanning direction were performed. Rotation of the scanning angle led to the rotation of the observed periodic structure (Fig S1, more details on these control experiments are provided in the supplementary materials to this paper). Thus, it was concluded that the observed structure was due to the nature of the sample, and was not an artifact of the piezoscanner.

In previous studies of muscovite (Kuwahara, 1999; Liu and Brown 1997, Leiro 2014), the authors correlated the periodic structure images obtained by AFM with the structure of the surface of the silica tetrahedral sheet. Ferrage et al. (2006) investigated the surface of talc crystals and also brought it in correspondence with the periodic structure of the silica tetrahedral sheet. Teschke et al. (2010) proposed that when performing the AFM scanning of clay mineral, the surface layer of H_2O molecules should be taken into account in the interpretation of the signal. They indeed observed, on a mica surface, a periodic structure of 0.45 nm that corresponded to the ice-Ih

(hexagonal) type, predicted by atomistic simulations (Odelius, 1997; Wang et al., 2005a, 2005b). More detailed studies of the first several layers of water on the mica surface were performed using oscillatory AFM techniques, which allow to construct force curves (Fukuma et al., 2005, 2010; Kimura et al., 2010; Kobayashi, et al., 2013). Using MD simulations, Kobayashi et al. (2016) investigated the interaction between a carbon nanotube (as an AFM probe) and a mica surface and evaluated the contribution of various forces to such interaction, thus allowing them to construct a density map of water molecules in the first and second hydration layers of the surface.

Hydration layers could be not taken in account if one identify reflections in the FFTs of high-resolution electron microscopy study of montmorillonite (Drummy et al., 2005). Present AFM experiments were performed under ambient relative humidity conditions of 20% and above. Under these conditions, it is expected that approximately one to two monolayers of water are present at clay surface (Cases et al., 1992).

In the present study, we performed MD simulations of hydrated mica and montmorillonite surfaces for better understanding and interpretation of the nature of these periodic structures. The ClayFF force field used in the simulations is primarily based on electrostatic interactions between partial charges assigned to individual atoms and Lennard-Jones (12-6) function (Cygan et al., 2004). Assuming that the main contribution to the interaction of the silicon nitride cantilever and the surface of montmorillonite or mica is due to the electrostatic interactions (e.g., Gan, 2009), we calculated the electrostatic potential induced by the distribution of atomic charges at every point in space and compared the two-dimensional maps of the electrostatic potential along the clay surface with the AFM images.

To calculate the surface electrostatic potential from MD simulations, the model supercell was divided into a three-dimensional mesh with a resolution of $0.03\times0.03\times0.03$ nm^3. For each element of the mesh the electrostatic potential was computed according to:

209 $$U = \frac{1}{4\pi\varepsilon}\sum_{k=1}^{n}\frac{q_k}{r_k}$$

210 (1)

211 where q_k – are the partial atomic charges of the ClayFF model (Cygan et al., 2004) and r_k – are the
212 instantaneous distances between this particular element of the mesh and the charged atom. The
213 calculation was performed every 10 ps along the equilibrium MD trajectory and the results were
214 then time-averaged over the entire trajectory.

215 The averaging of the electrostatic potential calculated along the (001) plane at different
216 distances from the solid/liquid interface over the entire MD-generated trajectory showed that, for
217 mica, the K^+ on the surface are well localized and could contribute significantly to the AFM signal.
218 This result is in agreement with previous findings using MD simulations (Kobayashi et al. 2016).
219 On the contrary, on the surface of Na-montmorillonite, the averaged contribution of the Na^+ to the
220 surface electrostatic potential is significantly blurred over the 1 ns time scale of the simulation
221 (Fig. 4), and it is thus unlikely that Na^+ on the montmorillonite surface contribute significantly to
222 the periodic patterns observed on AFM images.

223 Fast Fourier transform (FFT) of the periodic structures observed in high resolution the AFM
224 images were further compared with the FFT of the calculated electrostatic potential maps of the
225 first hydration layer obtained from MD simulations (Fig. 5). The FFT maps from the AFM images
226 and the calculated electrostatic maps are qualitatively similar. Their main difference is in the
227 absence of secondary peaks on the FFT maps from the AFM image due to experimental noise and/or
228 structural disorder such as bending, sligth variation in atomic positions, anisotropic displacement
229 factors, vacancies and isomorphic substitutions. The most intense contributions to the FFT maps
230 (dominant frequencies of the periodic signal) was assigned to the direction perpendicular to the
231 [010] crystallographic direction with a periodicity of ~0.45 nm, ~0.23 nm (1/2 and 1/4 of the *b*
232 crystallographic unit cell dimension, Fig. 5) and to the direction perpendicular to the [100] direction

233 with the periodicity of ~0.26 nm (1/2 of the *a* crystallographic unit cell dimension, Fig. 5).
234 Consequently, we assumed that the bright reflex on the FFT of the AFM images with the periodicity
235 of ~0.45 nm corresponded to the *b* direction of the particles.

236 To evaluate the relative abundances of different crystallographic edge surface orientations of
237 montmorillonite nanoparticles, the AFM images were rotated in such a way that the edge
238 perpendicular to the *b* direction was horizontal and became the reference vector for the angles
239 characterizing the remaining edges (Fig. 6). Note that this method does not allow us to distinguish
240 the edges perpendicular to the direction [110] from the edges perpendicular to the opposite direction
241 $[\bar{1}\bar{1}0]$ and the like.

242 In the case of a single monocrystalline particle, the crystallographic directions defining the
243 orientations of its edge surfaces can be determined from AFM images on a nanometer scale (Fig. 6;
244 supplementary materials).

245

246 **Table 1.** Calculated relative ratios of the edge lengths for a typical montmorillonite particle shown
247 in Fig. 7, compared with the pyrophyllite particle edge ratios predicted by DFT
248 calculations using two different methods marked ΔE (minimization of the cleavage
249 energies) and ΔG (minimization of Gibbs free energies) (Lavikainen at al. 2015).

Edge surface normal to	Angle (°)	Edge surface area ratios based on		
		AFM (this work)	DFT calculations from (Lavikainen at al. 2015)	
			ΔE	ΔG
[010]	0	0.20	0.33	0.29
[130]	30	0.09	0.00	0.00
[110]	60	0.56	0.61	0.69

[100]	90	0.03	0.06	0.02
unidentified	-	0.12	-	-

To determine the ratio of the edge lengths corresponding to each specific orientation, the results were averaged over a large number of measurements. Figure 7 shows the total histogram of the resulting distribution measured for individual 26 particles. The surfaces normal to the [110] direction was significantly more prevalent than the surfaces normal to the [010] direction (Fig. 7 and Table 1), in good agreement with the predictions from recent atomistic simulations (Lavikainen at al. 2015, Newton et al., 2016).

CONCLUSIONS

The combination of atomic-force microscopy (AFM) measurements and molecular dynamics (MD) computer simulations enabled to identify and quantify the relative abundances of the most frequently occurring edge surfaces of montmorillonite. The total edge specific surface area was evaluated to be $SSA_{Edge} \sim 4.3 \pm 0.2$ m^2g^{-1}. MD simulations were used to construct a 3D map of the electrostatic potential around montmorillonite particles placed on the surface of muscovite (mimicking the conditions of experimental observations). Fourier transformation of the calculated 3D electrostatic potential maps made it possible to identify characteristic reflexes at ~0.45 nm and ~0.23 nm on the Fourier-transformed experimental AFM images. The reflex at ~0.45 nm corresponds to the periodicity along the crystallographic *b* direction, while the reflex at ~0.26 nm corresponds to the periodicity along the crystallographic *a* direction. The knowledge of the particle orientations made it possible to quantify the relative abundance of crystallographic directions of the montmorillonite edge surfaces. The edge surface normal to the [110] and [010] crystallographic directions were found to be the most abundant (~60%, ~20% respectively), in agreement with previously published estimations based on DFT simulations. According to our measurements, the

contribution of the edge surface normal to the [130] to the total SSA_{Edge} is equal to 10%, a value which exceeds the prediction made using DFT simulations.

ACKNOWLEDGMENTS

This collaborative project between BRGM and SUBATECH was supported by the GL CTEC Program funded by the French National Radioactive Waste Management Agency (ANDRA) and by the industrial chair "Storage and Disposal of Radioactive Waste" at the Institut Mines-Télécom Atlantique (funded by ANDRA, ORANO, and EDF). A.G.K. also acknowledges support of the HSE University Basic Research Program in the framework of the Russian Academic Excellence Project "5-100".

REFERENCES

Assemi, S., Sharma, S., Tadjiki, S., Prisbrey, K., Ranville, J., Miller, J.D., 2015. Effect of Surface Charge and Elemental Composition on the Swelling and Delamination of Montmorillonite Nanoclays Using Sedimentation Field-flow Fractionation and Mass Spectroscopy. Clays and Clay Minerals 63, 457–468. https://doi.org/10.1346/CCMN.2015.0630604

ANDRA, 2005, Evaluation of the feasibility of a geological repository in an argillaceous formation, Dossier 2005, Argile – Synthesis, ANDRA, Châtenay-Malabry, 241pp.

Bauer, A., Velde, B., and Gaupp, R. (2016). Experimental constraints on illite crystal morphology. Clay Minerals *35*, 587–597.

Bickmore, B.R., Rosso, K.M., Nagy, K.L., Cygan, R.T., and Tadanier, C.J. (2003). Ab Initio Determination of Edge Surface Structures for Dioctahedral 2:1 Phyllosilicates: Implications for Acid-Base Reactivity. Clays Clay Miner. *51*, 359–371.

Borisover, M. and Davis, J. A. Chapter 2 - Adsorption of inorganic and organic solutes by clay minerals. In Tournassat, C.; Steefel, C. I.; Bourg, I. C. & Bergaya, F. (Eds.) Natural and Engineered Clay Barriers, Elsevier, 2015, 6, 33-70

Bourg, I.C., Sposito, G., and Bourg, A.C.M. (2007). Modeling the acid–base surface chemistry of montmorillonite. Journal of Colloid and Interface Science *312*, 297–310.

Cases, J.M., Berend, I., Besson, G., Francois, M., Uriot, J.P., Thomas, F., Poirier, J.E. (1992). Mechanism of adsorption and desorption of water vapor by homoionic montmorillonite. 1. The sodium-exchanged form. Langmuir *8*, 2730–2739. https://doi.org/10.1021/la00047a025

Churakov, S.V. (2006). Ab Initio Study of Sorption on Pyrophyllite: Structure and Acidity of the Edge Sites. J. Phys. Chem. B *110*, 4135–4146.

Cygan, R. T., Liang, J. J., Kalinichev, A. G. (2004).Molecular models of hydroxide, oxyhydroxide, and clay phases and the development of a general force field. J. Phys. Chem. B *108*, 1255–1266.

309 Drits, V. A., Guggenheim, S., Zviagina, B. B., and Kogure, T. (2012). Structures of the 2:1 layers
310 of pyrophyllite and talc. *Clays Clay Miner.* 60, 574–587.

311 Erlandsson, R., Hadziioannou, G., Mate, C.M., McClelland, G.M., and Chiang, S. (1988). Atomic
312 scale friction between the muscovite mica cleavage plane and a tungsten tip. J. Chem. Phys.
313 *89*, 5190–5193.

314 Everett A. Jenne (1998). Adsorption of Metals by Geomedia (Elsevier).

315 Ferrage, E., Seine, G., Gaillot, A.-C., Petit, S., De Parseval, P., Boudet, A., Lanson, B., Ferret, J.,
316 and Martin, F. (2006). Structure of the {001} talc surface as seen by atomic force microscopy:
317 comparison with X-ray and electron diffraction results. Eur. J. Mineral *18*, 483–491.

318 Filonov, A., Gavrilko, D., and Yaminsky, I. (2001). FemtoScan SPM Image damaging by the tip
319 during scanning. Processing Software Manual.

320 Fukuma, T., Kobayashi, K., Matsushige, K., and Yamada, H. (2005). True atomic resolution in
321 liquid by frequency-modulation atomic force microscopy. Appl. Phys. Lett. *87*, 034101.

322 Fukuma Takeshi, Ueda Yasumasa, Yoshioka Shunsuke, and Asakawa Hitoshi (2010). Atomic-scale
323 distribution of water molecules at the mica-water interface visualized by three-dimensional
324 scanning force microscopy. Phys. Rev. Lett *104*, 016101.

325 Le Forestier, L., Muller, F., Villieras, F., and Pelletier, M. (2010). Textural and hydration properties
326 of a synthetic montmorillonite compared with a natural Na-exchanged clay analogue. Applied
327 Clay Science *48*, 18–25.

328 Gan, Y. (2009) Atomic and subnanometer resolution in ambient conditions by atomic force
329 microscopy. Surface Science Reports *64*, 99-121.

330 Gates, W. P., Bouazza, A., Churchman, G. J. (2009). Bentonite clay keeps pollutants at bay.
331 Elements, *5*, 105-110.

332 Güven, N. (2001). Mica structure and fibrous growth of illite. Clays and Clay Minerals *49*, 189–
333 196.

Kimura, K., Ido, S., Oyabu, N., Kobayashi, K., Hirata, Y., Imai, T., and Yamada, H. (2010). Visualizing water molecule distribution by atomic force microscopy. J Chem Phys *132*, 194705.

Kobayashi, K., Oyabu, N., Kimura, K., Ido, S., Suzuki, K., Imai, T., Tagami, K., Tsukada, M., and Yamada, H. (2013). Visualization of hydration layers on muscovite mica in aqueous solution by frequency-modulation atomic force microscopy. J. Chem. Phys. *138*, 184704.

Kobayashi, K., Liang, Y., Amano, K., Murata, S., Matsuoka, T., Takahashi, S., Nishi, N., and Sakka, T. (2016). Molecular dynamics simulation of atomic force microscopy at the water–muscovite interface: Hydration layer structure and force analysis. Langmuir *32*, 3608–3616.

Kuwahara, Y. (1999). Muscovite surface structure imaged by fluid contact mode AFM. Phys Chem Min *26*, 198–205.

Kwon, K.D., and Newton, A.G. (2016). Structure and stability of pyrophyllite edge surfaces: Effect of temperature and water chemical potential. Geochim. Cosmochim. Acta *190*, 100–114.

Lavikainen, L.P., Hirvi, J.T., Kasa, S., Schatz, T., and Pakkanen, T.A. (2015). Stability of dioctahedral 2:1 phyllosilicate edge structures based on pyrophyllite models. Theor Chem Acc *134*, 112.

Leiro, J.A., Torhola, M., and Laajalehto, K. (2017). The AFM method in studies of muscovite mica and galena surfaces. Journal of Physics and Chemistry of Solids *100*, 40–44.

Liu, Z.H., and Brown, N.M.D. (1997). The influence of imaging conditions on the appearance of lattice-resolved AFM images of mica surfaces. J. Phys. D: Appl. Phys. *30*, 2503–2508.

Liu, X., Lu, X., Wang, R., Zhou, H., and Xu, S. (2008). Surface complexes of acetate on edge surfaces of 2:1 type phyllosilicate: Insights from density functional theory calculation. Geochimica et Cosmochimica Acta *72*, 5896–5907.

Liu, X., Lu, X., Meijer, E.J., Wang, R., and Zhou, H. (2012). Atomic-scale structures of interfaces between phyllosilicate edges and water. Geochimica et Cosmochimica Acta *81*, 56–68.

Liu, X., Lu, X., Sprik, M., Cheng, J., Meijer, E.J., and Wang, R. (2013). Acidity of edge surface sites of montmorillonite and kaolinite. Geochimica et Cosmochimica Acta *117*, 180–190.

Liu, X., Cheng, J., Sprik, M., Lu, X., and Wang, R. (2014). Surface acidity of 2:1-type dioctahedral clay minerals from first principles molecular dynamics simulations. Geochimica et Cosmochimica Acta *140*, 410–417.

Liu, X., Cheng, J., Sprik, M., Lu, X., and Wang, R. (2015a). Interfacial structures and acidity of edge surfaces of ferruginous smectites. Geochimica et Cosmochimica Acta *168*, 293–301.

Liu, X., Lu, X., Cheng, J., Sprik, M., and Wang, R. (2015b). Temperature dependence of interfacial structures and acidity of clay edge surfaces. Geochimica et Cosmochimica Acta *160*, 91–99.

Loganathan, N. and Kalinichev, A. G., 2017. Quantifying the mechanisms of site-specific ion exchange at an inhomogeneously charged surface: Case of Cs^+/K^+ on hydrated muscovite mica. Journal of Physical Chemistry C 121, 7829–7836.

Marti, O., Colchero, J., and Mlynek, J. (1990). Combined scanning force and friction microscopy of mica. Nanotechnology *1*, 141.

Marty, N.C.M., Fritz, B., Clément, A., and Michau, N. (2010). Modelling the long term alteration of the engineered bentonite barrier in an underground radioactive waste repository. Applied Clay Science *47*, 82–90.

Marty, N.C.M., Cama, J., Sato, T., Chino, D., Villiéras, F., Razafitianamaharavo, A., Brendlé, J., Giffaut, E., Soler, J.M., Gaucher, E.C., et al. (2011). Dissolution kinetics of synthetic Na-smectite. An integrated experimental approach. Geochimica et Cosmochimica Acta *75*, 5849–5864.

Newton, A.G., and Sposito, G. (2015). Molecular dynamics simulations of pyrophyllite edge surfaces: Structure, surface energies, and solvent accessibility. Clays Clay Miner *63*, 277–289.

Newton, A.G., Kwon, K.D., and Cheong, D.-K. (2016). Edge Structure of Montmorillonite from Atomistic Simulations. Minerals *6*, 25.

385 Ngouana W., B.F., and Kalinichev, A.G. (2014). Structural arrangements of isomorphic
386 substitutions in smectites: Molecular simulation of the swelling properties, interlayer
387 structure, and dynamics of hydrated Cs–montmorillonite revisited with new clay models. J.
388 Phys. Chem. C *118*, 12758–12773.
389 Odelius, M., Bernasconi, M., and Parrinello, M. (1997). Two Dimensional Ice Adsorbed on Mica
390 Surface. Phys. Rev. Lett. *78*, 2855–2858.
391 Orucoglu, E., Tournassat, C., Robinet, J.-C., Madé, B., and Lundy, M. (2018). From experimental
392 variability to the sorption related retention parameters necessary for performance assessment
393 models for nuclear waste disposal systems: The example of Pb adsorption on clay minerals.
394 Applied Clay Science *163*, 20–32.
395 Plimpton, S. (1995). Fast Parallel Algorithms for Short-Range Molecular Dynamics. Journal of
396 Computational Physics *117*, 1–19.
397 Reinholdt, M.X., Hubert, F., Faurel, M., Tertre, E., Razafitianamaharavo, A., Francius, G., Prêt,
398 D., Petit, S., Béré, E., Pelletier, M., et al. (2013). Morphological properties of vermiculite
399 particles in size-selected fractions obtained by sonication. Applied Clay Science *77–78*, 18–
400 32.
401 Reischl, B., Raiteri, P., Gale, J.D., Rohl, A.L. (2019) Atomistic simulation of atomic force
402 microscopy imaging of hydration layers on calcite, dolomite, and magnesite surfaces.
403 J. Phys. Chem. C *123*, 14985-14992.
404 Rodriguez-Fortun, J.M., Orus, J., Alfonso, J., Buil, F., and Castellanos, J.A. (2011). Hysteresis in
405 piezoelectric actuators: Modeling and compensation. IFAC Proceedings Vol. *44*, 5237–5242.
406 Siretanu, I., Ende, D. van den, and Mugele, F. (2016). Atomic structure and surface defects at
407 mineral-water interfaces probed by in situ atomic force microscopy. Nanoscale *8*, 8220–8227.
408 Tachi, Y., and Yotsuji, K. (2014). Diffusion and sorption of Cs^+, Na^+, I^- and HTO in compacted
409 sodium montmorillonite as a function of porewater salinity: Integrated sorption and diffusion
410 model. Geochimica et Cosmochimica Acta *132*, 75–93.

411 Teschke, O., Filho, J.F.V., and de Souza, E.F. (2010). Imaging two-dimensional ice-like structures
412 at room temperature. Chemical Physics Letters *485*, 133–136.
413 Tournassat, C., and Appelo, C.A.J. (2011). Modelling approaches for anion-exclusion in compacted
414 Na-bentonite. Geochimica et Cosmochimica Acta *75*, 3698–3710.
415 Tournassat, C., Davis, J.A., Chiaberge, C., Grangeon, S., and Bourg, I.C. (2016). Modeling the
416 acid–base properties of montmorillonite edge surfaces. Environ. Sci. Technol. *50*, 13436–
417 13445.
418 Tournassat, C., Grangeon, S., Leroy, P., and Giffaut, E. (2013). Modeling specific pH dependent
419 sorption of divalent metals on montmorillonite surfaces. A review of pitfalls, recent
420 achievements and current challenges. Am J Sci *313*, 395–451.
421 Tournassat, C., Neaman, A., Villiéras, F., Bosbach, D., and Charlet, L. (2003). Nanomorphology
422 of montmorillonite particles: Estimation of the clay edge sorption site density by low-pressure
423 gas adsorption and AFM observations. American Mineralogist *88*, 1989–1995.
424 Tsipursky, S. I. and Drits, V. (1984) The distribution of octahedral cations in the 2:1 layers of
425 dioctahedral smectites studied by oblique-texture electron diffraction. Clay Minerals, 19,
426 177-193
427 Umeda, K., Zivanovic, L., Kobayashi, K., Ritala, J., Kominami, H., Spijker, P., Foster, A.S.,
428 Yamada, H. (2017). Atomic-resolution three-dimensional hydration structures on a
429 heterogeneously charged surface. Nature Communications *8*, 2111.
430 Wang, J. W.; Kalinichev, A. G.; Kirkpatrick, R. J.; Cygan, R. T. (2005a) Structure, energetics, and
431 dynamics of water adsorbed on the muscovite (001) surface: A molecular dynamics
432 simulation. Journal of Physical Chemistry B, 109, 15893-15905.
433 Wang, J. W.; Kalinichev, A. G.; Kirkpatrick, R. J. (2005b) Structure and decompression melting of
434 a novel, high-pressure nanoconfined 2-D ice. J. Phys. Chem. B, 109, 14308-14313.

435 Yokoyama, S., Kuroda, M., and Sato, T. (2005). Atomic force microscopy study of montmorillonite
436 dissolution under highly alkaline conditions. Clays Clay Miner *53*, 147–154.

437 Zhang, C., Liu, X., Lu, X., He, M., Meijer, E. J., and Wang, R. (2017) Surface complexation of
438 heavy metal cations on clay edges: insights from first principles molecular dynamics
439 simulation of Ni(II). Geochimica et Cosmochimica Acta 203, 54-68.

440 Zhang, C., Liu, X., Lu, X., and He, M. (2018) Complexation of heavy metal cations on clay edges
441 at elevated temperatures. Chemical Geology 479, 36-46.

442

443

444 **FIGURES AND TABLE CAPTIONS**

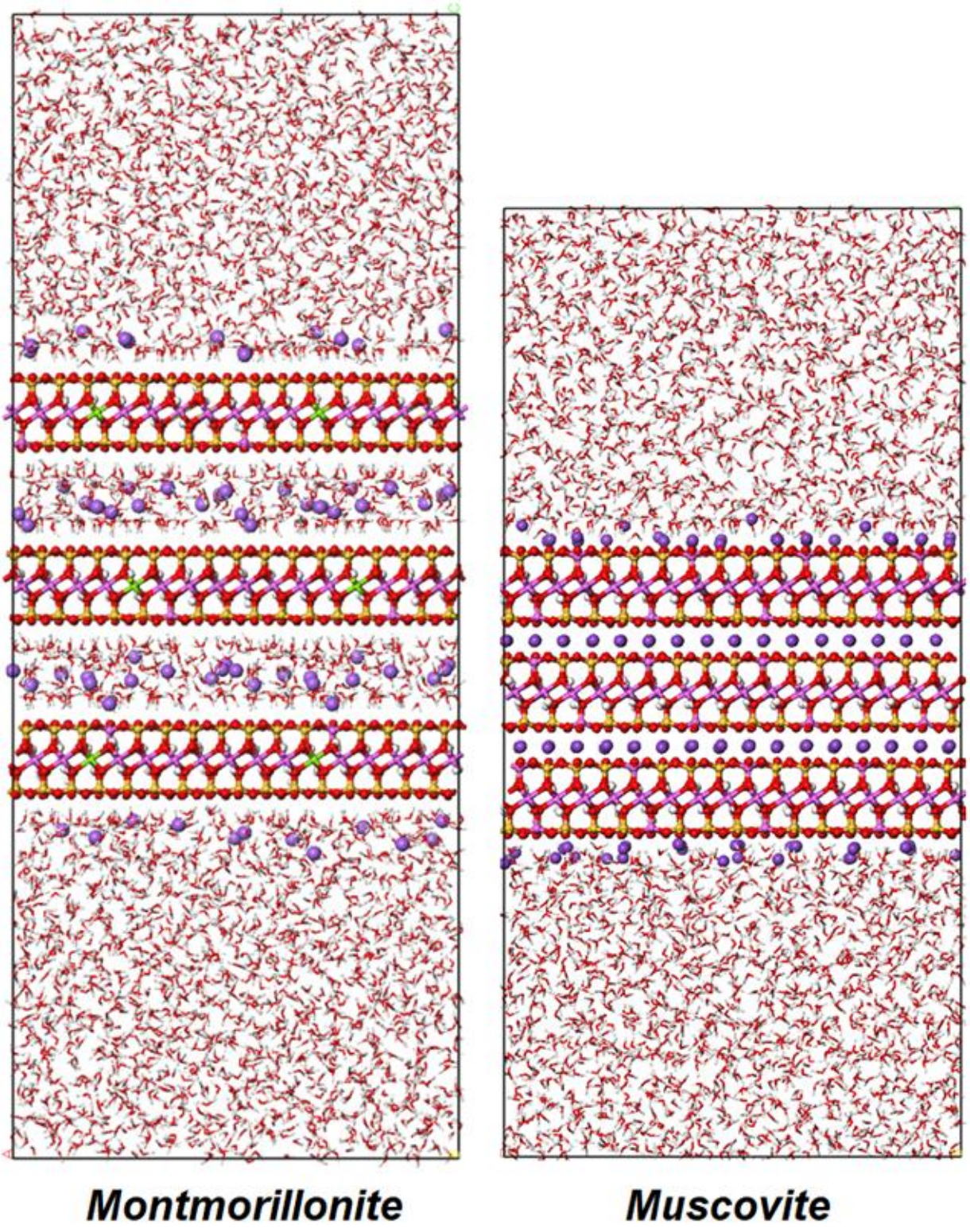

445

446 Figure 1. General initial views of the simulation supercells of montmorillonite (left) and muscovite

447 (right) used in the MD simulations.

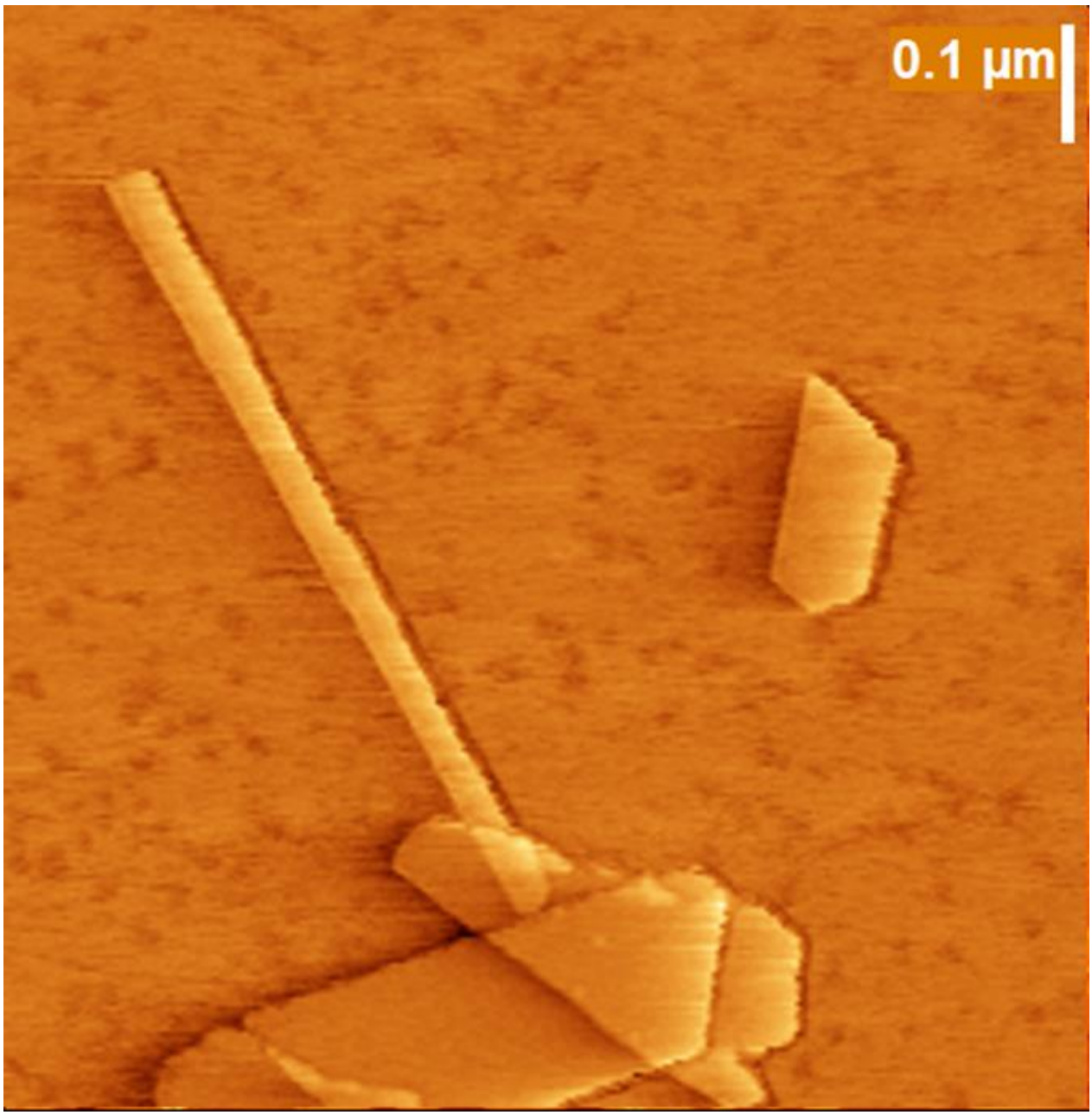

Figure 2. Contact mode deflection AFM image of a clay particle with lath shape, and other particles with well-defined straight boundaries.

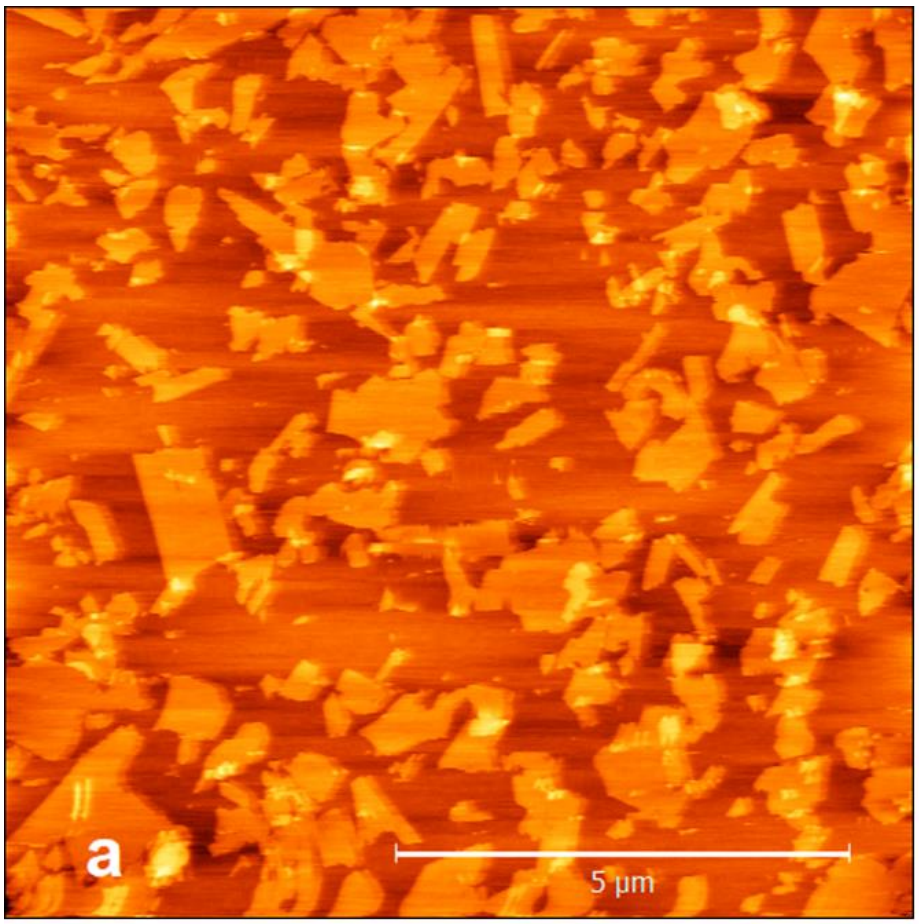

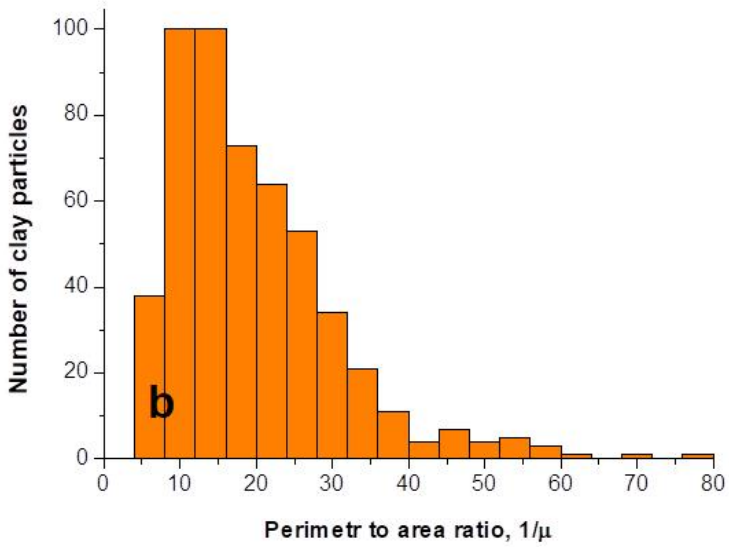

451

452 Figure 3. (a) Contact mode height AFM image of montmorillonite particles on the surface of
453 muscovite. (b) Histogram of perimeter-to-area ratio distribution of the measured montmorillonite
454 particles.

455

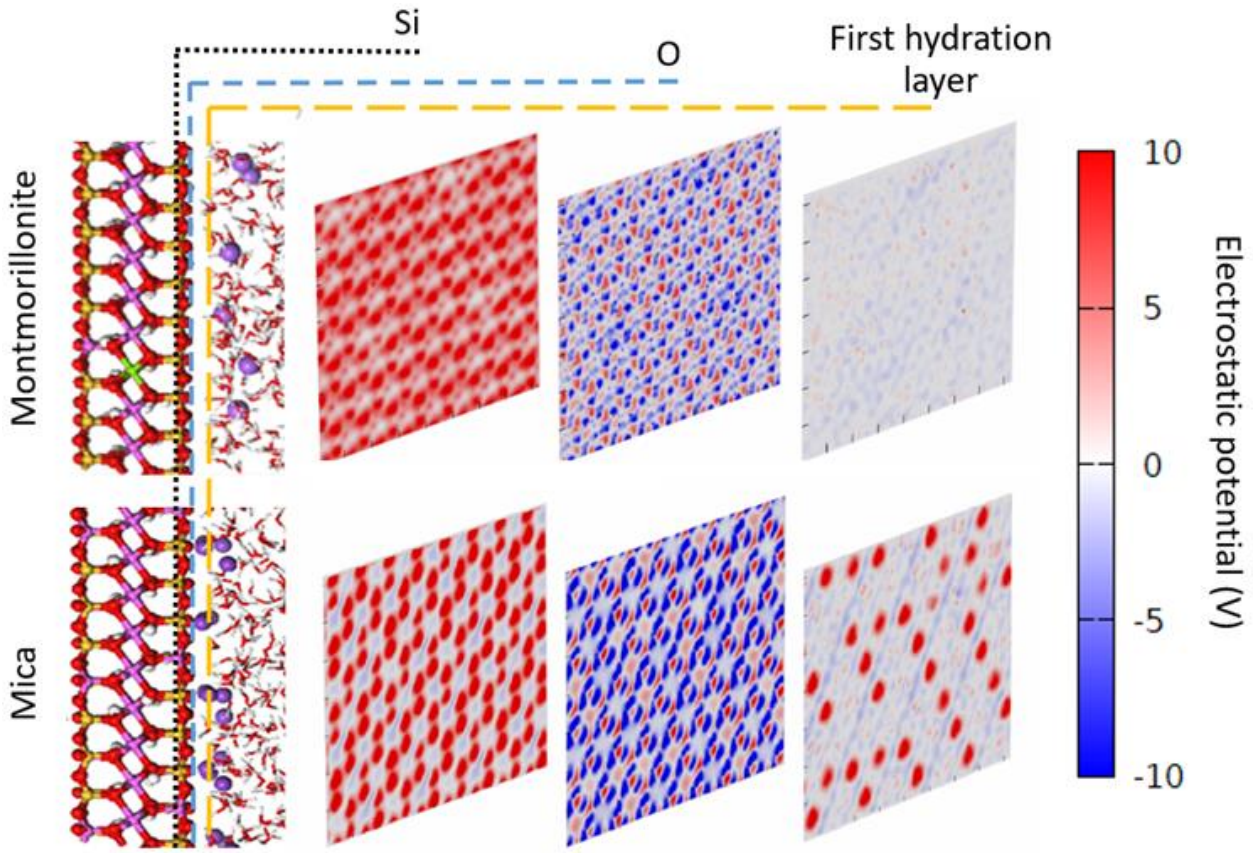

Figure 4. Maps of the time-averaged electrostatic potential (V) parallel to the (001) surface at different cross sections calculated from MD simulations. Maps drawn through the planes of time-averaged positions of the Si and O atoms of the clay show a honeycomb-like structure. The maps of electrostatic forces in the first hydrated surface, defined here as the plane 0.3 nm away from the plane of the surface O atoms, are much less ordered. In the case of montmorillonite, the honeycomb-like pattern is just barely distinguishable at the same color scale. In the case of the first hydration layer on the surface of the mica, the main contribution to the electrostatic forces is due to the absorbed K^+ counterions.

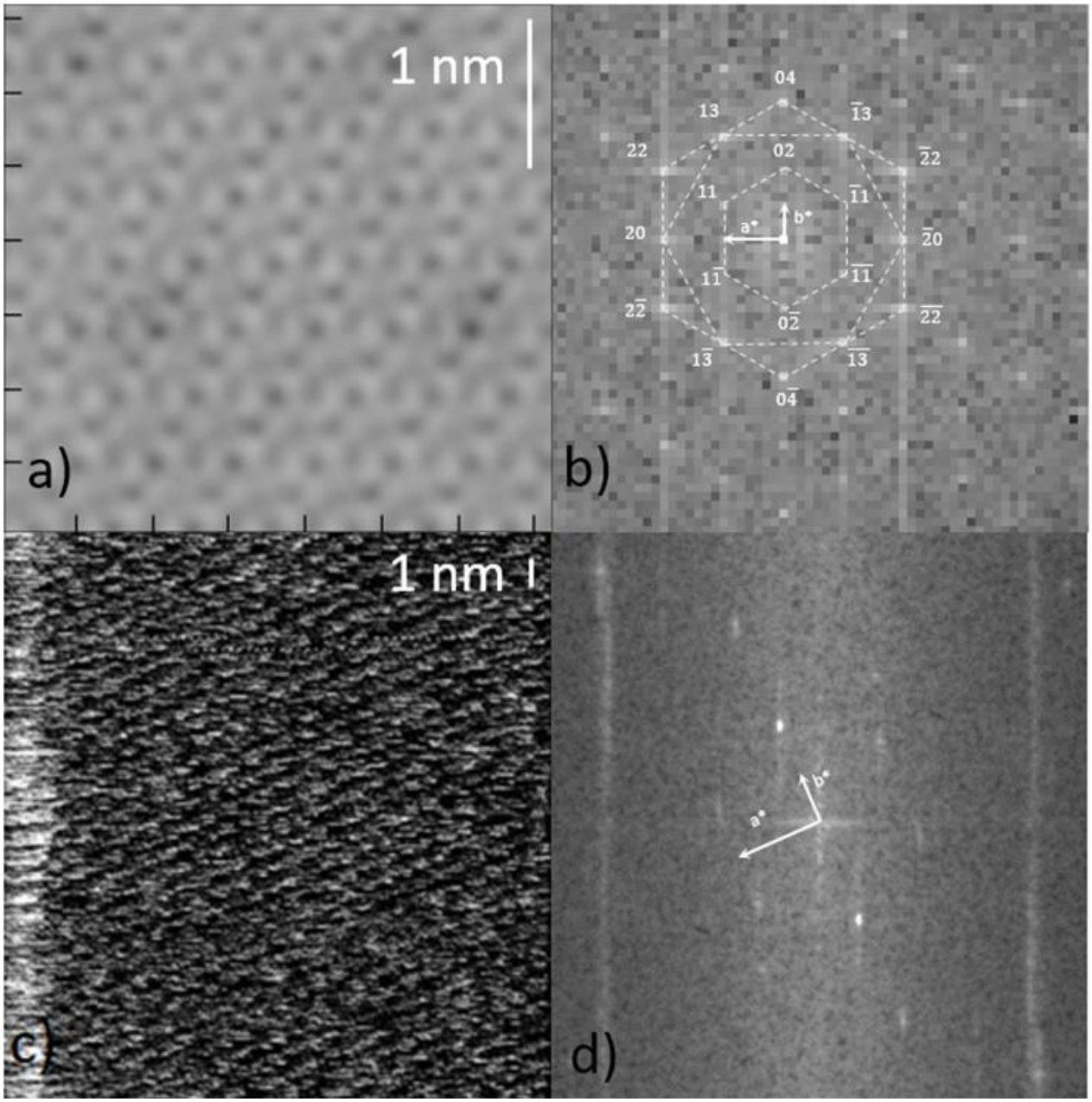

Figure 5. Electrostatic potential distribution into first hydration layer along the basal (001) surface of montmorillonite calculated from MD simulations (a) and its fast Fourier transform (b), compared with an friction mode AFM-image of the montmorillonite 15×15 nm^2 surface (c) and its fast Fourier transform (d). In both FFT images one pair of reflections corresponding to a spatial periodicity of 0.45 nm is brighter than the other two pairs. We are using this brightest pair to define the crystallographic direction *b*.

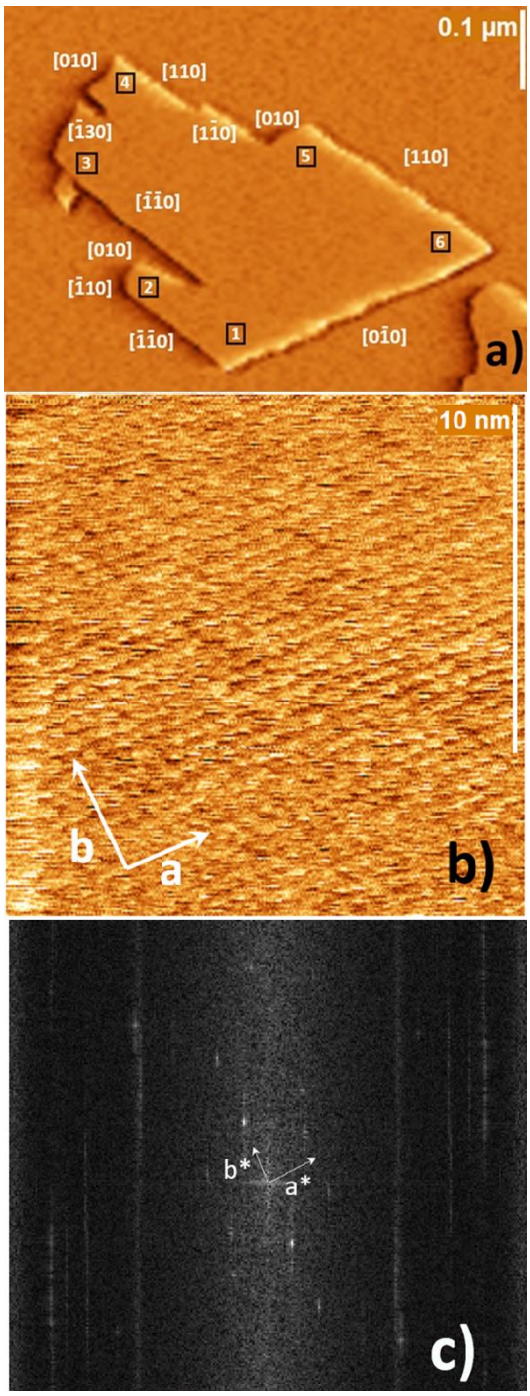

Figure 6. (a) AFM image of the montmorillonite particle; (b) atomic resolution AFM image captured on the square spot #1; (c) FFT of (b). The direction of vector *b* is chosen according to the brightest reflex with the 0.46 nm period, the sign of the vector is determined arbitrarily. To prove that the particle is, indeed, monocrystalline, several other atomic resolution images corresponding to spots #2-6 were obtained and provided as supplementary materials. The crystallographic indexes of the edge surfaces were defined by measuring the angle between the direction of the edge and the vector *b* .

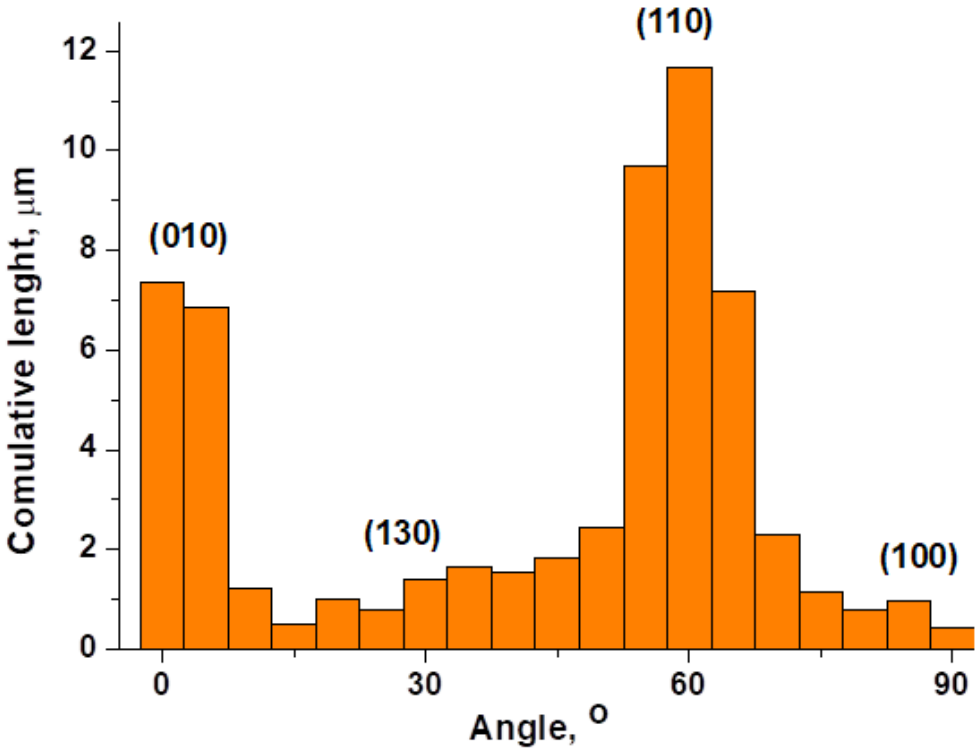

480

481 Figure 7. Distribution histogram of montmorillonite particle edge surface orientations, with
482 cumulative total lengths of the correspondingly oriented edges.

483

484

485

486

487

488

489

490

	Angle (°)	Edge surface area ratios based on

Edge surface normal to		AFM (this work)	DFT calculations from (Lavikainen at al. 2015)	
			ΔE	ΔG
[010]	0	0.20	0.33	0.29
[130]	30	0.09	0.00	0.00
[110]	60	0.56	0.61	0.69
[100]	90	0.03	0.06	0.02
unidentified	-	0.12	-	-

Table 1. Calculated relative ratios of the edge lengths for a typical montmorillonite particle shown in Fig. 7, compared with the pyrophyllite particle edge ratios predicted by DFT calculations using two different methods marked ΔE (minimization of the cleavage energies) and ΔG (minimization of Gibbs free energies) (Lavikainen et al., 2015).